

Mapping atomic and diffuse interstellar band absorption across the Magellanic Clouds and the Milky Way

Mandy Bailey^{1,2}, Jacco Th. van Loon¹, Peter J. Sarre³ and John E. Beckman^{4,5,6}

¹*Lennard-Jones Laboratories, Keele University, ST5 5BG, UK*

²*Astrophysics Research Institute, Liverpool John Moores University, IC2, Liverpool Science Park, Liverpool L3 5RF, UK*

³*School of Chemistry, The University of Nottingham, University Park, Nottingham, NG7 2RD, UK*

⁴*Instituto Astrofísica de Canarias, E-38205 La Laguna, Tenerife, Spain*

⁵*Department of Astrophysics, University of La Laguna, E-38205 La Laguna, Tenerife, Spain*

⁶*C.S.I.C., E-28040 Madrid, Spain*

Submitted: 28 August 2015; accepted: 17 September 2015

ABSTRACT

Diffuse interstellar bands (DIBs) trace warm neutral and weakly-ionized diffuse interstellar medium (ISM). Here we present a dedicated, high signal-to-noise spectroscopic survey of two of the strongest DIBs, at 5780 and 5797 Å, in optical spectra of 666 early-type stars in the Small and Large Magellanic Clouds, along with measurements of the atomic Na I D and Ca II K lines. The resulting maps show for the first time the distribution of DIB carriers across large swathes of galaxies, as well as the foreground Milky Way ISM. We confirm the association of the 5797 Å DIB with neutral gas, and the 5780 Å DIB with more translucent gas, generally tracing the star-forming regions within the Magellanic Clouds. Likewise, the Na I D line traces the denser ISM whereas the Ca II K line traces the more diffuse, warmer gas. The Ca II K line has an additional component at ~ 200 – 220 km s^{−1} seen towards both Magellanic Clouds; this may be associated with a pan-Magellanic halo. Both the atomic lines and DIBs show sub-pc-scale structure in the Galactic foreground absorption; the 5780 and 5797 Å DIBs show very little correlation on these small scales, as do the Ca II K and Na I D lines. This suggests that good correlations between the 5780 and 5797 Å DIBs, or between Ca II K and Na I D, arise from the superposition of multiple interstellar structures. Similarity in behaviour between DIBs and Na I in the SMC, LMC and Milky Way suggests the abundance of DIB carriers scales in proportion to metallicity.

Key words: galaxies: ISM – ISM: atoms – ISM: lines and bands – ISM: molecules – ISM: structure – Magellanic Clouds

1 INTRODUCTION

The interstellar medium (ISM) plays a critical role in the star formation and chemical evolution of galaxies. Yet a full understanding remains elusive, with it being seen only in part or under special conditions. This is true in particular for the molecular component, as molecular hydrogen is virtually invisible, challenging our ability to investigate how and when atomic gas becomes molecular. Even though the exact nature of their presumed molecular carriers is unknown¹, the diffuse interstellar bands (DIBs) they generally cause in the spectra of stars are a powerful probe of the molecular ISM and the atomic–molecular interfaces.

The Magellanic Clouds are two nearby (≈ 60 and 50

kpc for the SMC and LMC, respectively) interacting, gas-rich dwarf galaxies with sub-solar ISM metallicities ($Z \approx \frac{1}{5}$ and $\frac{1}{2} Z_{\odot}$ for the SMC and LMC, respectively). The recession velocities (~ 150 km s^{−1} for the SMC and 250–300 km s^{−1} for the LMC) result in Doppler shifts with respect to absorption in the Milky Way of ~ 3.5 Å in the SMC and ~ 5.5 Å in the LMC at visible wavelengths. While some DIBs are broader than this, many are narrow enough to separate the Magellanic from the foreground Galactic absorption (Jenkins & Désert 1994). This is the case particularly for the 5780 and 5797 Å DIBs, which are intrinsically strong and their ratio is a clear diagnostic of exposure to UV irradiation and/or high electron density.

Hutchings (1966) was the first to report a DIB in the Magellanic Clouds, viz. the broad 4430 Å band. Subsequent detections and upper limits were obtained by Blades & Madore (1979) and Houziaux, Nandy & Morgan (1980,

¹ Campbell et al. (2015) have recently reported confirmation of two near-IR diffuse bands as due to gas-phase C₆₀⁺.

1985). Ehrenfreund et al. (2002) first detected the 5780 and 5797 Å DIBs in the SMC. While the UV radiation field seems to be the dominant factor affecting the relative strengths of DIBs in the Magellanic Clouds (Cox et al. 2006), other local conditions matter too (Welty et al. 2006), with Cox et al. (2007) highlighting metallicity effects both through reduced shielding against UV light and possibly directly through elemental depletions. Following pioneering efforts by van Loon et al. (2009) to map DIBs across the sky, van Loon et al. (2013) presented such maps towards the Tarantula Nebula in the LMC, showing a clear relation of DIBs with the diffuse ISM and with the radiation field.

Here we present high signal-to-noise spectra from a dedicated campaign to map the 5780 and 5797 Å DIBs and the Ca II K and Na I D lines across most of the SMC and a large part of the LMC. These are the first maps of this kind, revealing how the DIB carriers relate to the neutral and weakly ionized gas, the diffuse and star-forming ISM, and UV-shielded and irradiated conditions in these metal-poor environments. At the same time, we also map the Galactic foreground absorption, revealing small-scale structure in all these tracers, as well as Ca II K absorption arising in intermediate- and high-velocity clouds which are probably located in the Galactic Halo.

2 DATA

2.1 Observations

The observations were carried out with the 3.9-m Anglo-Australian Telescope (AAT) at Siding Spring, Australia, during 3–6 November 2011 (programmes ATAC/10B/51 and AAT/11B/17; PI: J.Th. van Loon). The two-degree field (2dF) 400-fibre positioning system was used in conjunction with the AAO spectrograph mounted at the Coudé focus, benefitting from a wide-field corrector and an atmospheric dispersion compensator. The spectrograph has a dichroic beam-splitter allowing simultaneous observation of a “blue” and a “red” spectrum created with volume phase holographic (VPH) reflection gratings. Each spectrum was sampled with an e2v CCD with 2k pixels along the spectral and 4k pixels along the spatial direction.

We used the 3200B and 2000R gratings with the 570-nm dichroic, with the central wavelength set to 3935 Å for the blue arm and 5840 Å for the red arm. This yielded a spectral resolving power of $R = \lambda/\Delta\lambda \approx 8,000$ (38 km s^{-1}), covering wavelength ranges of 3779–4084 Å in the central fibre and 3751–4054 Å in the end fibres in the blue, and 5569–6101 Å in the central fibre and 5528–6056 Å in the end fibres in the red.

The SMC field was observed in the first half of the night and the LMC field in the second. The weather conditions deteriorated throughout the observing run, with seeing from $1''.3$ to $\sim 3''$ and increasing levels of cloud cover. Eventually, the SMC and LMC fields received total integration times of 12.5 hr and 13 hr, respectively, all split into individual 30-minute integrations.

Before and after each night the following calibration measurements were performed: bias (electronic offset), dark current level, arc lamp exposures for wavelength calibration, and flat field observations on the sky and dome – the latter

employing 20-W lamps for the red and 75-W lamps for the blue.

2.2 Target selection

The targets, fiducial stars (for acquisition) and sky positions are shown in figure 1; they were selected from the Magellanic Clouds Photometric Survey (Zaritsky et al. 2002). While the best targets for the study of interstellar absorption are early-type stars, which are bright and have relatively few and weak spectral features, their colours may have been reddened by interstellar dust and we must avoid too heavy a bias against such sight-lines. Therefore, initially targets were selected to have $13.5 < V < 15$ mag, and $-1 < (B - V) < 0.5$ mag for the SMC but $-1 < (B - V) < 0.4$ mag for the LMC. A higher priority was given to stars with a reddening-free colour (Johnson 1963; Massey 2007) $Q = (U - B) - 0.72 \times (B - V) < -0.4$ mag (red symbols in Fig. 1). When plotted using also the reddening-free Wesenheit index $W = V - 3.1 \times (B - V)$ (Madore 1982, using the canonical value $R_V = 3.1$) the early- and later-type stars separate much more clearly than in the unreddened colour-magnitude diagram. Indeed, the early-type stars trace the star forming regions whereas the later-type stars are concentrated towards the LMC bar in the South-West corner of the 2° field (Fig. 1). The later-type stars, while not ideal targets for our study, were not excluded from selection entirely as they could still fill some fibres that could not otherwise be allocated. In Appendix A we describe the distribution over known spectral types, confirming the success of our selection strategy. Fiducials (green triangles in Fig. 1) were selected from 13th-mag (V) stars with $0.3 < (B - V) < 0.6$ mag. Targets or fiducial stars were rejected if other stars were known to affect the signal within the fibre significantly. Sky positions (blue dots in Fig. 1) were chosen to be clear of known stars within or near to the fibre.

The CONFIGURE software was used to allocate fibres to targets, up to 8 fiducial stars, and 25 empty positions for sky measurements to be subtracted from the target stars’ spectra. An annealing scheme was employed to optimise the target allocation, yielding ≈ 350 targets per 2dF field. The final selection of observed targets – 338 in the SMC and 328 in the LMC – is shown in figure 2 and table 1 (made available in full at CDS).

2.3 Data processing

The data were processed using the 2dFDR tool (Lewis et al. 2002). The reduction steps include: bias subtraction, dark subtraction, flat-fielding, tram-line mapping of the (curved) spectra on the CCD, spectra extraction, arc lamp spectral line identification, wavelength calibration, fibre throughput calibration and sky subtraction. The blue and red spectra are processed separately.

Accurate subtraction of sky emission lines can be a challenge for fibre-fed spectrographs. While the standard sky subtraction in 2dFDR produced good results, the very strong telluric Na I D lines were not always removed entirely (see also the high resolution fibre-fed spectra in van Loon et al. 2013). The residual telluric emission was accounted for at the analysis stage (see next section).

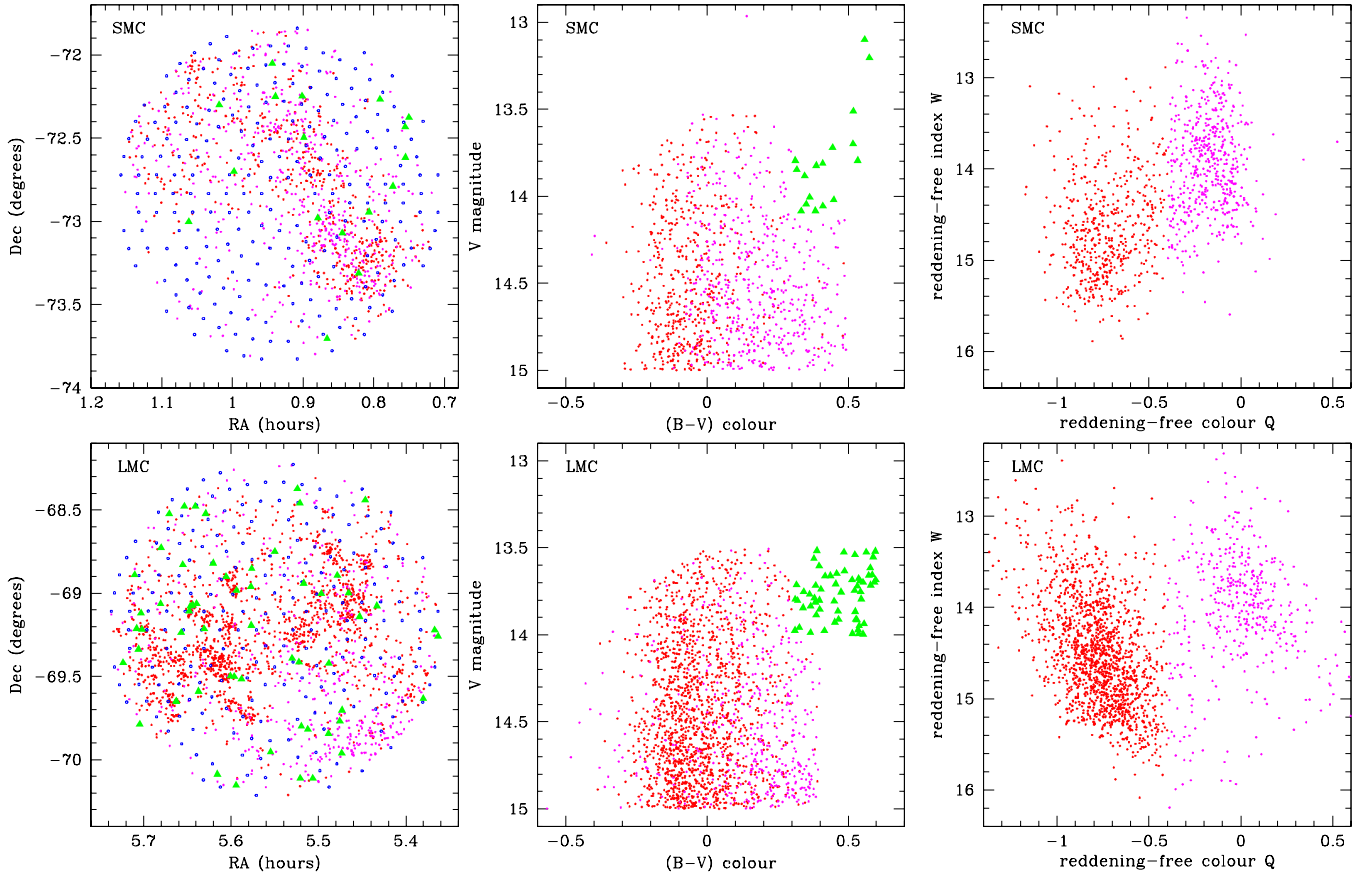


Figure 1. Distribution of SMC (*top row*) and LMC (*bottom row*) targets (high priority: red; low priority: magenta), fiducials (green triangles) and sky positions (blue dots) on the sky (*left*), in optical colour and brightness (*middle*) and in reddening free indices (*right*).

Table 1. List of observed targets. Only the first three objects in each of the SMC and LMC are shown here. The ID numbers are from our own target lists. Both equatorial and Galactic coordinates are given as the latter are useful in interpreting the foreground absorption. Spectral types and luminosity classes are based on a literature search and only available for 174 SMC and 61 LMC targets (see Appendix A). B- and V-band photometry are from Zaritsky et al. (2002). The full version of this table is available on CDS.

ID	RA (^h ^m ^s)	Dec (° ' ")	<i>l</i> (°)	<i>b</i> (°)	<i>B</i> (mag)	<i>V</i> (mag)	spectral type
<i>SMC:</i>							
983	1 05 49.02	−72 48 18.0	301.44836	−44.28177	14.58	14.79	-
942	1 04 05.97	−72 43 50.9	301.61804	−44.36510	14.02	14.16	-
762	0 58 11.26	−72 36 10.0	302.22449	−44.51616	14.36	14.21	-
<i>LMC:</i>							
1856	5 41 16.56	−69 14 02.2	279.59109	−31.43029	14.31	14.20	-
1913	5 41 59.34	−69 14 56.5	279.60104	−31.36586	15.11	14.97	-
1281	5 36 09.39	−69 13 58.0	279.65109	−31.88117	14.58	14.50	-

The spectra from all of the nights were processed individually but then combined using custom-written routines in IDL: first they were rectified and normalised, then the root-mean-square noise level (standard deviation in a line-free region) was determined, the reciprocal value of which acted as the weight in averaging the spectra.

3 ANALYSIS

In this work we concentrate on the ISM tracers in the spectra, viz. the Ca II K (the H component 34.8 Å further to the

red is obliterated by He), Na I D₁ and D₂, and the 5780 Å and 5797 Å DIBs, both for the SMC and LMC as well as the Galactic foreground.

The spectral regions around the above absorption features were fitted using a combination of a first-order polynomial (baseline) and Gaussian functions. The actual fitting was coded in IDL using the MPFIT routines.

The constraints on the fitting are summarised in table 2. In particular, the wavelength of the 5797 Å DIB was guided by that of the stronger 5780 Å DIB and allowed to vary less to avoid spurious results. Likewise, the wavelength and width of the D₁ (red) component of the Na I doublet were

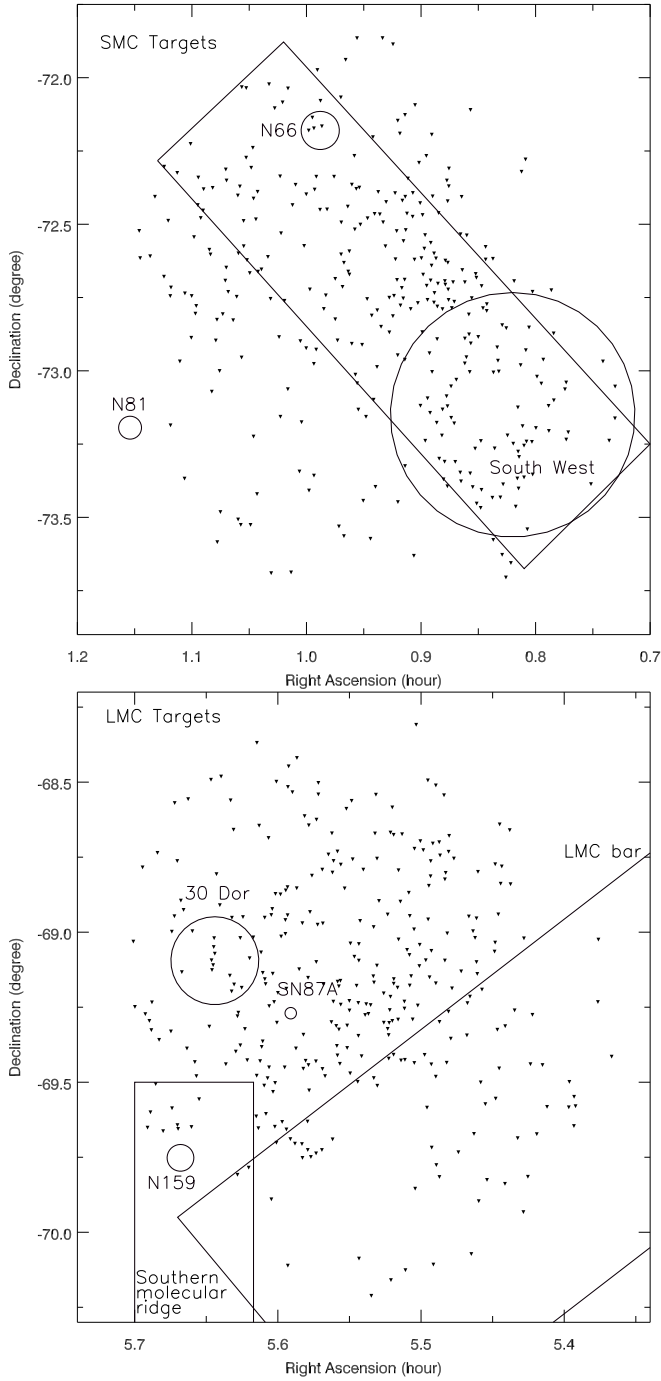


Figure 2. Distribution of observed targets in the SMC (*top*) and LMC (*bottom*). Some features of interest are indicated, including 30 Doradus, SN 1987A, etc.

tied to that of the stronger D₂ (blue) component – except in the LMC where the opposite strategy was used because its D₂ line coincides with the Galactic foreground D₁ line. Overlapping components were fitted simultaneously. The peaks of the Gaussian functions were forced to be negative, but an additional positive-valued double-Gaussian function (with a fixed separation of 5.97 Å) was included around the rest wavelengths of the Na I D lines to account for telluric emission. It was noted that the SMC and LMC components of the Ca II K line often showed a second component. Towards

Table 2. Overview of the Gaussian fitting constraints, in Å.

Feature	λ_0		σ	
	guess	range	guess	range
<i>SMC, internal:</i>				
Ca II K (blue)	3935.6	± 2.00	0.2	0.10 – 0.40
Ca II K (red)	3936.6	± 1.00	0.2	0.10 – 0.40
5780 DIB	5783.6	± 1.00	0.6	0.036 – 0.90
5797 DIB	$\lambda_{5780} + 16.5$	± 0.75	0.5	0.25 – 1.00
Na I D ₂	5893.0	± 2.00	0.5	0.25 – 1.00
Na I D ₁	$\lambda_{D2} + 5.97$		σ_{D2}	
<i>Galactic, in SMC direction:</i>				
Ca II K	3933.6	± 2.00	0.3	0.15 – 0.60
5780 DIB	5780.1	± 1.00	0.6	0.036 – 0.90
5797 DIB	$\lambda_{5780} + 16.5$	± 0.75	0.5	0.25 – 1.00
Na I D ₂	5890.0	± 2.00	0.5	0.25 – 1.00
Na I D ₁	$\lambda_{D2} + 5.97$		σ_{D2}	
<i>LMC, internal:</i>				
Ca II K (blue)	3937.0	± 1.00	0.2	0.12 – 0.30
Ca II K (red)	3937.5	± 0.50	0.2	0.12 – 0.30
5780 DIB	5786.0	± 1.00	0.6	0.036 – 0.90
5797 DIB	$\lambda_{5780} + 16.5$	± 0.75	0.5	0.25 – 1.00
Na I D ₂	$\lambda_{D1} - 5.97$		σ_{D1}	
Na I D ₁	5901.0	± 2.00	0.5	0.25 – 1.00
<i>Galactic, in LMC direction:</i>				
Ca II K (blue)	3933.6	± 1.00	0.2	0.12 – 0.30
Ca II K (red)	3935.0	± 0.50	0.2	0.12 – 0.30
5780 DIB	5780.8	± 1.00	0.6	0.036 – 0.90
5797 DIB	$\lambda_{5780} + 16.5$	± 0.75	0.5	0.25 – 1.00
Na I D ₂	5890.0	± 2.00	0.5	0.25 – 1.00
Na I D ₁	$\lambda_{D2} + 5.97$		σ_{D2}	

the LMC, a second component was also seen in the Galactic foreground.

The equivalent width EW was determined by integrating the Gaussian function:

$$EW = \int_{-\infty}^{\infty} A \exp\left(-\frac{(\lambda - \lambda_0)^2}{2\sigma^2}\right) d\lambda = A\sigma\sqrt{2\pi}, \quad (1)$$

where A is the peak intensity, λ_0 the central wavelength and σ the width (with the Full Width at Half Maximum, $FWHM = 2.355\sigma$). The errors e_0 resulting from MPFIT-EXPR were scaled according to the χ^2 deviations from the fit and the degrees of freedom f (the number of spectral elements minus the number of fitting parameters) as in:

$$e = e_0 \sqrt{\chi^2/f} \quad (2)$$

Hence the error in the equivalent width is obtained from:

$$e[EW] = \sqrt{2\pi((e[A]\sigma)^2 + (Ae[\sigma])^2)} \quad (3)$$

All spectra and fits were vetted by eye, guided by the value for $EW/e[EW]$, and only fits deemed reliable were retained. Rejected data include a few spectra with broadened Ca II K absorption arising in the stellar photosphere (Appendix A presents an overview of the spectral types and their mostly negligible effect on the measured equivalent widths). The full tables of measurements are available at CDS, with the first three entries shown in tables 3 and 4.

Three of our targets (all in the LMC) have also been subject of measurement of the 5780 Å DIB in previous studies. Our target 1491 (BI 253) was measured in a high resolution spectrum by Welty et al. (2006); their $EW_{5780} =$

Table 3. Spectral line measurements for SMC sight-lines. EW stands for equivalent width; $e[EW]$ its uncertainty. Flags f are 1 or 0 for a detection or non-detection, respectively; The full, transposed version of this table is available on CDS.

ID	983	942	762
<i>SMC, internal:</i>			
$EW_{\text{CaII K blue}} (\text{\AA})$	0.224	0.185	0.310
$e[EW]_{\text{CaII K blue}} (\text{\AA})$	0.019	0.005	0.006
$(EW/e[EW])_{\text{CaII K blue}}$	11.6	36.1	48.5
$EW_{\text{CaII K red}} (\text{\AA})$	0.040	0.041	0.154
$e[EW]_{\text{CaII K red}} (\text{\AA})$	0.012	0.004	0.005
$(EW/e[EW])_{\text{CaII K red}}$	3.4	9.1	30.5
$EW_{5780} (\text{\AA})$	-	0.006	0.052
$e[EW]_{5780} (\text{\AA})$	-	0.001	0.002
$(EW/e[EW])_{5780}$	-	6.5	23.3
$EW_{5797} (\text{\AA})$	0.016	-	0.009
$e[EW]_{5797} (\text{\AA})$	0.007	-	0.001
$(EW/e[EW])_{5797}$	2.3	-	10.7
$EW_{\text{NaID2}} (\text{\AA})$	0.096	0.096	0.246
$EW_{\text{NaID1}} (\text{\AA})$	0.129	0.064	0.164
$e[EW]_{\text{NaID2}} (\text{\AA})$	0.008	0.004	0.005
$e[EW]_{\text{NaID1}} (\text{\AA})$	0.008	0.004	0.004
$(EW/e[EW])_{\text{NaID2}}$	12.2	21.7	46.2
$(EW/e[EW])_{\text{NaID1}}$	16.0	18.0	38.2
$f_{\text{CaII K blue}}$	1	1	1
f_{5780}	0	0	1
f_{5797}	0	0	1
f_{NaID}	0	1	1
<i>Galactic, in SMC direction:</i>			
$EW_{\text{CaII K}} (\text{\AA})$	0.190	0.126	0.088
$e[EW]_{\text{CaII K}} (\text{\AA})$	0.019	0.004	0.005
$(EW/e[EW])_{\text{CaII K}}$	10.0	31.4	19.0
$EW_{5780} (\text{\AA})$	0.033	0.024	0.022
$e[EW]_{5780} (\text{\AA})$	0.005	0.002	0.003
$(EW/e[EW])_{5780}$	6.7	13.7	7.6
$EW_{5797} (\text{\AA})$	0.016	0.013	0.025
$e[EW]_{5797} (\text{\AA})$	0.002	0.002	0.002
$(EW/e[EW])_{5797}$	6.8	5.6	10.9
$EW_{\text{NaID2}} (\text{\AA})$	0.136	0.086	0.209
$EW_{\text{NaID1}} (\text{\AA})$	0.048	0.056	0.148
$e[EW]_{\text{NaID2}} (\text{\AA})$	0.008	0.006	0.012
$e[EW]_{\text{NaID1}} (\text{\AA})$	0.005	0.005	0.011
$(EW/e[EW])_{\text{NaID2}}$	16.1	15.0	17.8
$(EW/e[EW])_{\text{NaID1}}$	9.2	11.5	13.9
$f_{\text{CaII K}}$	1	1	1
f_{5780}	0	0	0
f_{5797}	0	0	1
f_{NaID}	1	1	1

$0.075 \pm 0.016 \text{ \AA}$ agrees with our $EW_{5780} = 0.056 \pm 0.003 \text{ \AA}$. Our targets 1611 (VFTS 532) and 1625 (VFTS 604) had been measured in similar high resolution spectra by van Loon et al. (2013); they got $EW_{5780} = 0.175 \pm 0.007 \text{ \AA}$ for star 1611 compared to our $EW_{5780} = 0.194 \pm 0.006 \text{ \AA}$, and $EW_{5780} = 0.123 \pm 0.009 \text{ \AA}$ for star 1625 compared to our $EW_{5780} = 0.137 \pm 0.003 \text{ \AA}$. All three comparisons are consistent within $2-3\sigma$. Reassuringly, the measurements of the sodium lines also agreed very well: for star 1611, $EW_{\text{NaID1}} = 0.463$ and 0.466 \AA in van Loon et al. (2013) and this work, respectively, while for star 1625 these values were $EW_{\text{NaID1}} = 0.467$ and 0.451 \AA , respectively.

Table 4. As table 3 but for LMC sight-lines.

ID	1856	1913	1281
<i>LMC, internal:</i>			
$EW_{\text{CaII K blue}} (\text{\AA})$	0.243	0.255	0.035
$e[EW]_{\text{CaII K blue}} (\text{\AA})$	0.005	0.007	0.003
$(EW/e[EW])_{\text{CaII K blue}}$	45.1	37.3	11.3
$EW_{\text{CaII K red}} (\text{\AA})$	0.169	0.190	0.168
$e[EW]_{\text{CaII K red}} (\text{\AA})$	0.005	0.009	0.005
$(EW/e[EW])_{\text{CaII K red}}$	31.4	21.2	32.2
$EW_{5780} (\text{\AA})$	0.141	0.015	0.051
$e[EW]_{5780} (\text{\AA})$	0.003	0.003	0.003
$(EW/e[EW])_{5780}$	55.5	4.8	20.2
$EW_{5797} (\text{\AA})$	0.030	0.017	0.012
$e[EW]_{5797} (\text{\AA})$	0.003	0.002	0.004
$(EW/e[EW])_{5797}$	11.8	10.2	3.5
$EW_{\text{NaID2}} (\text{\AA})$	0.544	0.524	0.308
$EW_{\text{NaID1}} (\text{\AA})$	0.424	0.216	0.232
$e[EW]_{\text{NaID2}} (\text{\AA})$	0.013	0.049	0.017
$e[EW]_{\text{NaID1}} (\text{\AA})$	0.006	0.005	0.005
$(EW/e[EW])_{\text{NaID2}}$	41.6	10.8	17.6
$(EW/e[EW])_{\text{NaID1}}$	66.5	39.7	46.1
$f_{\text{CaII K blue}}$	1	1	1
f_{5780}	1	0	1
f_{5797}	1	0	0
f_{NaID}	1	1	1
<i>Galactic, in LMC direction:</i>			
$EW_{\text{CaII K blue}} (\text{\AA})$	0.128	0.118	0.127
$e[EW]_{\text{CaII K blue}} (\text{\AA})$	0.005	0.004	0.006
$(EW/e[EW])_{\text{CaII K blue}}$	28.5	30.6	22.6
$EW_{\text{CaII K red}} (\text{\AA})$	0.034	0.026	0.121
$e[EW]_{\text{CaII K red}} (\text{\AA})$	0.005	0.006	0.004
$(EW/e[EW])_{\text{CaII K red}}$	7.5	4.6	33.7
$EW_{5780} (\text{\AA})$	0.017	0.027	0.010
$e[EW]_{5780} (\text{\AA})$	0.001	0.004	0.001
$(EW/e[EW])_{5780}$	11.6	6.6	9.5
$EW_{5797} (\text{\AA})$	0.009	0.016	0.005
$e[EW]_{5797} (\text{\AA})$	0.001	0.004	0.002
$(EW/e[EW])_{5797}$	7.2	4.3	2.9
$EW_{\text{NaID2}} (\text{\AA})$	0.195	0.171	0.312
$EW_{\text{NaID1}} (\text{\AA})$	0.254	0.099	0.257
$e[EW]_{\text{NaID2}} (\text{\AA})$	0.041	0.019	0.186
$e[EW]_{\text{NaID1}} (\text{\AA})$	0.061	0.015	0.154
$(EW/e[EW])_{\text{NaID2}}$	4.7	9.0	1.7
$(EW/e[EW])_{\text{NaID1}}$	4.2	6.4	1.7
$f_{\text{CaII K blue}}$	1	1	1
f_{5780}	1	1	1
f_{5797}	0	0	0
f_{NaID}	1	1	1

4 RESULTS

The average line profiles are shown in figure 3 (with the fits overplotted in red). From the fitted line shape, two velocity components of the Ca II K line are clearly visible in the Galactic foreground towards the LMC (Fig. 3e). Many spectra recorded towards individual stars also showed a second component internal to the SMC and LMC. The redshift of the LMC is large enough for its 5780 \AA DIB to be separated from that of the Galactic foreground (Fig. 3f). Towards the SMC the two velocity components are blended (Fig. 3b), but simultaneous fitting of two Gaussian functions worked well in accounting for their respective contributions. The narrower 5797 \AA DIB is resolved both towards the LMC

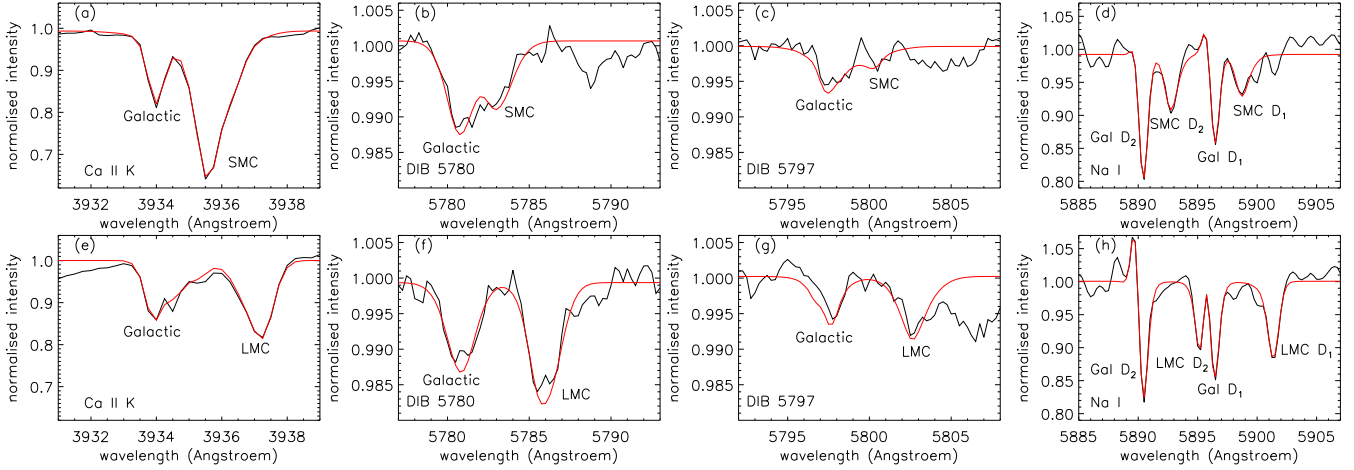


Figure 3. Average spectra for the SMC (*top row*) and LMC (*bottom row*) around the (*from left to right*): Ca II K, 5780 Å DIB, 5797 Å DIB and Na I D lines. The average fits are overplotted in red.

(Fig. 3g) and towards the SMC (Fig. 3c). The Na I D lines are well separated for the SMC (Fig. 3d) but towards the LMC the LMC D₂ component is close to the D₁ component of the Galactic foreground absorption (Fig. 3h). But again, simultaneous fitting worked well in resolving the two components. This is confirmed in the maps we show later, which – as expected – are very different for the different components.

While the spectral resolving power – and intrinsic width of the DIBs – did not allow us to identify multiple kinematic components other than (sometimes) a second one in the Ca II K, it is very likely that multiple kinematic components are present in all absorption features and sight-lines (cf. van Loon et al. 2013). Likewise, the Ca II K and Na I D absorption may be saturated in some of these components, and an increase of their equivalent width can be caused by stronger line wings as well as additional kinematic components. The D₁ line has half the intrinsic strength of that of the D₂ line and should therefore be less affected by saturation effects. While we caution against the use of the equivalent widths of the Ca II K and Na I D lines in an absolute sense, a comparative analysis can still be meaningful.

Remarkably, the Ca II K absorption towards the SMC is relatively strong compared to the Galactic foreground and LMC sight-lines; the DIBs are considerably weaker, though it must be said that the bulk of the absorption within the SMC is concentrated in areas much smaller than the 2° field and individual sight-lines can show quite strong DIBs.

4.1 Correlations

Figures 4–6 show plots of the EW of the 5780 vs. 5797 Å DIBs, 5780 Å DIB vs. Na I D₁ and 5797 Å DIB vs. Na I D₁, respectively. (Almost) no correlation was discernible between the DIBs and Ca II K. Plotted are not only the secure detections in both relevant features, but also (with different colours/symbols) less certain detections and non-detections. While some outliers and some of the scatter are due to uncertainties, there are clear positive correlations between the 5780 and 5797 Å DIBs and with Na I D but with real (intrinsic) scatter also. The equivalent width of the Na I D₁ line grows slower than in proportion to column density because

of saturation effects, giving the false impression of accelerated growth of the DIBs.

The Galactic foreground shows little difference between the SMC and LMC directions, but the SMC itself clearly has far fewer sight-lines with strong DIB absorption than the LMC (Fig. 4). Strong DIB absorption is seen internal to the SMC towards star 135 (SMC 10196 in Massey 2002) in the centre of the South-Western star-forming complex: $EW_{5797} = 0.079$ Å and $EW_{5780} = 0.280$ Å. The Na I D absorption is also strong in that direction. This sight-line passes in between the LHA-115 N25 OB association and the SMC-B23 molecular cloud; possibly it crosses the irradiated skin of a dense cloud, which may explain the strong DIB absorption. Similar strength of DIB absorption is seen at several locations within the LMC; the correlation appears to be saturating at $EW_{5780} \approx 0.30$ Å while the 5797 Å DIB continues to strengthen beyond $EW_{5797} > 0.1$ Å. The two stars that show the strongest 5797 Å DIB in figure 4 are both located within the Tarantula Nebula (cf. van Loon et al. 2013).

In Table 5 the results are summarised from a linear regression analysis and a Student *t* test for the 5780 and 5797 Å DIBs: the correlation is significant if $t > t_{\text{critical}}$, where

$$t = r \sqrt{\frac{N-2}{1-r^2}} \quad (4)$$

with correlation coefficient *r* and *N* data points (*N* – 2 degrees of freedom in this case). Hence we conclude that a good DIB–DIB correlation is seen within the SMC and LMC but that the Galactic foreground is probably too transparent to show a significant correlation. The 5780/5797 DIB ratio is very similar between the SMC, LMC and the Local Bubble – where $EW_{5780} = 0.023(\pm 0.005) + 2.48(\pm 0.20) \times EW_{5797}$ (Bailey et al. 2015). There is a hint that the relation is steeper (relatively stronger 5780 Å DIB) in the SMC, which could be explained as due to a harsher radiation field from metal-poor stars (reduced line-blanketing) in a metal-poor ISM (reduced attenuation by dust), but this is only marginally significant.

Both the DIBs and Na I D are weaker in the SMC than in the LMC (Figs. 5 & 6), but they behave simi-

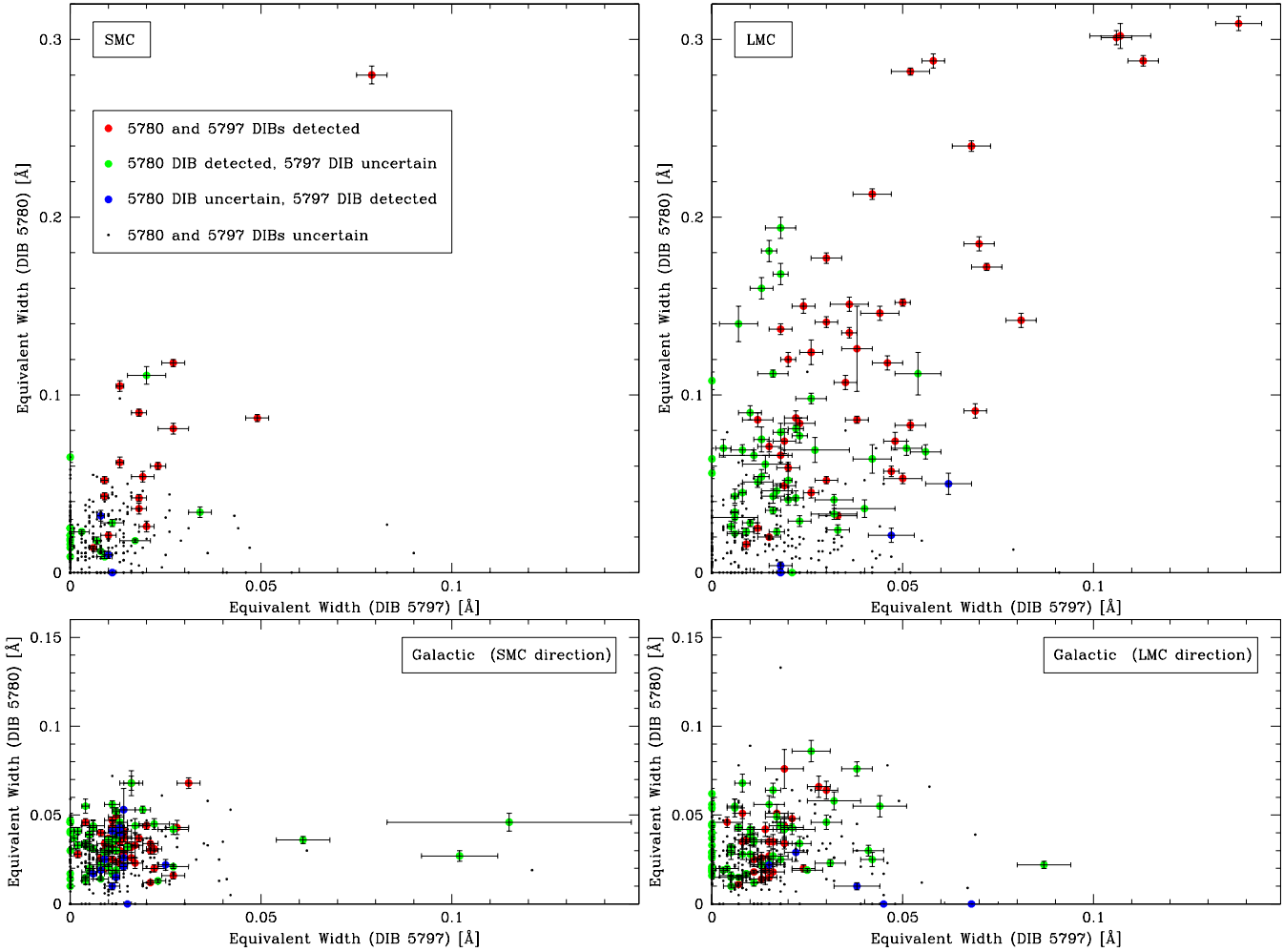


Figure 4. The equivalent width of the 5780 and 5797 Å DIBs for the SMC (*top left*), LMC (*top right*) and the Galactic foreground in the direction of the SMC (*bottom left*) and LMC (*bottom right*).

Table 5. Linear regression analysis of DIB–DIB correlations of the form $EW_{5780} = a + b \times EW_{5797}$ with correlation coefficient r . Where the Student t statistic is given, the critical value of t is for a 1% chance that the null hypothesis is true.

location	N	a (Å)	b	r	t	t_{critical}	verdict
SMC, internal	16	0.007 ± 0.005	2.93 ± 0.47	0.86	6.3	2.6	significant
LMC, internal	44	0.036 ± 0.013	2.17 ± 0.28	0.77	7.8	2.4	significant
Galactic, in SMC direction	38	0.032 ± 0.005	0.16 ± 0.31	0.09	0.5	2.4	insignificant
Galactic, in LMC direction	25	0.016 ± 0.003	1.24 ± 0.53	0.44	2.3	2.5	very marginal

larly. Both show what appears to be a threshold, or a more slowly picking up of DIB strength as Na I D_1 increases, around $EW_{\text{Na I D}_1} \sim 0.1$ Å. A similar behaviour was noticed in the Local Bubble (Bailey et al. 2015); it probably is due at least in part to the Na I D_1 saturating. The Galactic ISM is clearly more transparent in front of the SMC than in front of the LMC, which is probably related to the larger distance to the Galactic plane of the former. Quite strong absorption is seen in sight-lines close to the LMC in the Local Bubble survey (Bailey et al. 2015) though no sight-lines were observed by these authors within 10° of the SMC.

4.2 Maps

We constructed maps of the 5780 Å DIB, 5797 Å DIB, Ca II K and Na I D_2 equivalent widths within the SMC (Fig. 7), within the LMC (Fig. 8) and within the Galactic foreground (Figs. 9 & 10). We do not show the Na I D_1 maps but they look identical to the D_2 maps. We overlaid the positions of the stellar probes; as absorption was not always detected the maps are generally more sparsely sampled than the distribution of targets – which are already not distributed uniformly across the sky. The maps are filled in using triangulation, which preserves the true information (measurements) and does nothing but interpolate between

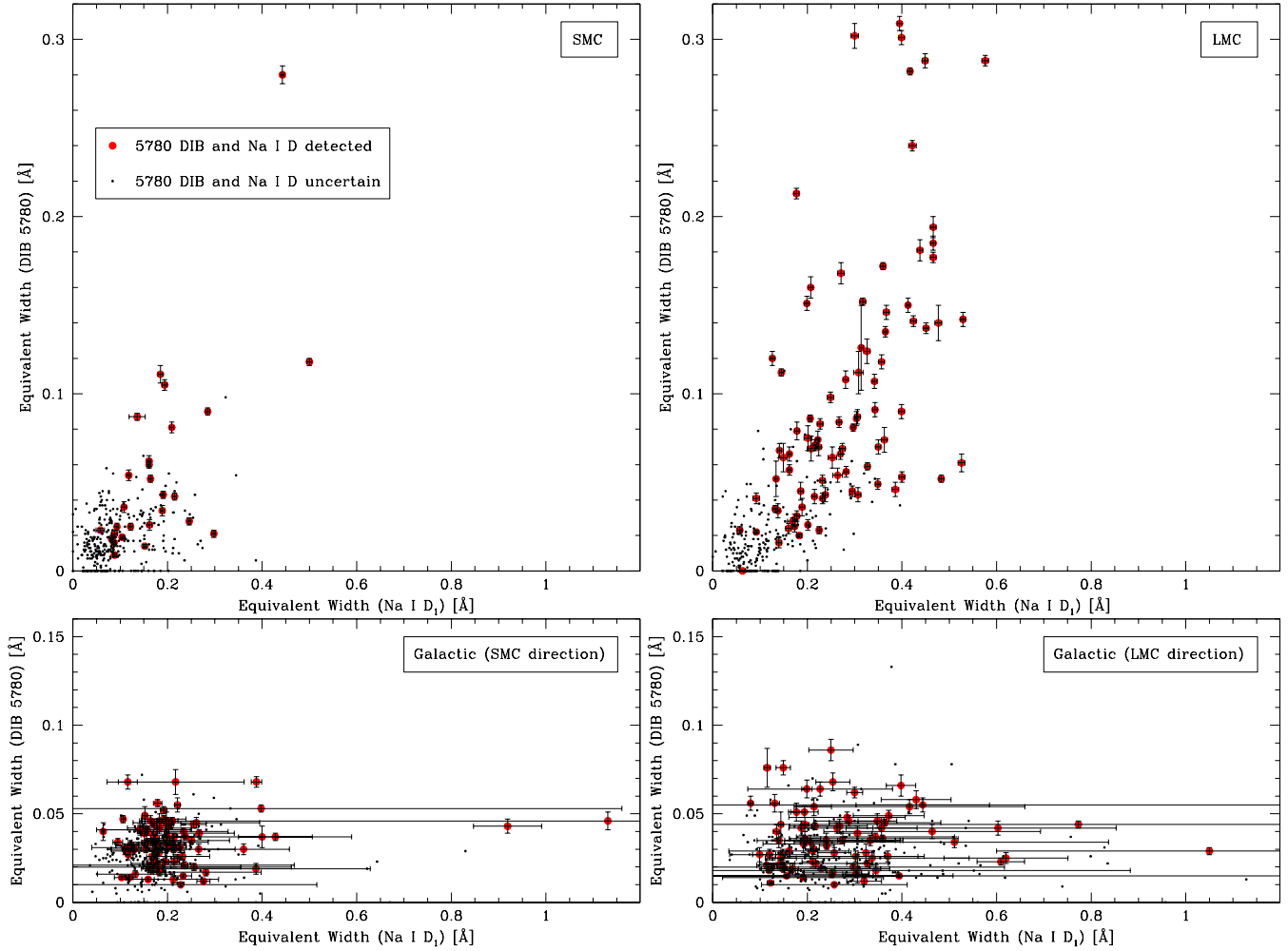


Figure 5. The equivalent width of the 5780 Å DIB versus that of the Na I D₁, for the SMC (*top left*), LMC (*top right*) and the Galactic foreground in the direction of the SMC (*bottom left*) and LMC (*bottom right*).

measurements without smoothing. The non-detections (magenta symbols) provide a meaningful addition to the maps as they outline areas of very low absorption. The SMC maps of the 5780 and 5797 Å DIBs are based on just 35 and 19 firm detections, respectively; for the LMC these are 91 and 48, respectively. The Ca II K line was detected in most sight-lines in both galaxies and the Na I D in about half of the sight-lines.

In the SMC (Fig. 7) the DIBs are strongly associated with the South-Western part of the SMC “bar”, where star formation is widespread. The EW_{5780}/EW_{5797} ratio appears to peak slightly offset from that region, perhaps tracing harsher conditions in the periphery of the star-forming molecular clouds as compared to those within the clouds. The South-Western part of the bar is also where Na I D peaks though it is detected more globally across the SMC. No DIBs were detected around the mini-starburst N 66 further North in the bar. The blue velocity component of Ca II K is detected across the SMC, tracing the generally hot, widely distributed gas typical of the metal-poor ISM in the SMC, but the red velocity component is concentrated towards the Wing, to the South-East of the bar. The red component might be situated behind the bulk of the stars,

hence the lack of detected absorption in this gas. There is no resemblance between the Ca II K maps and those of the DIBs, but it can be noted that where the DIBs are strongest the Ca II K is relatively weak. This shows a stronger affiliation of DIBs with Na I-bright material than with Ca II-bright material.

The LMC maps (Fig. 8) confirm this behaviour: The DIBs are strongest in molecular clouds within star-forming regions, but not too close to recently formed OB associations such as the central cluster R 136 (30 Doradus) within the Tarantula Nebula. This was also found in the DIB maps of the Tarantula Nebula by van Loon et al. (2013). The EW_{5780}/EW_{5797} ratio is high right at the location of R 136, as well as towards the West where the ISM becomes more diffuse (less self-shielded). The Na I D is concentrated in the same regions of great DIB strength, though more spread out. The Ca II K data are interesting: as in the SMC, the blue component is seen across the LMC also in areas with weak Na I D, though the densest parts tend to be situated in the East. The red component of Ca II K resembles the Na I D map more closely; here the East-West gradient is particularly evident, with the strongest absorption along the Eastern, leading edge of the LMC. Again we see a fair correspon-

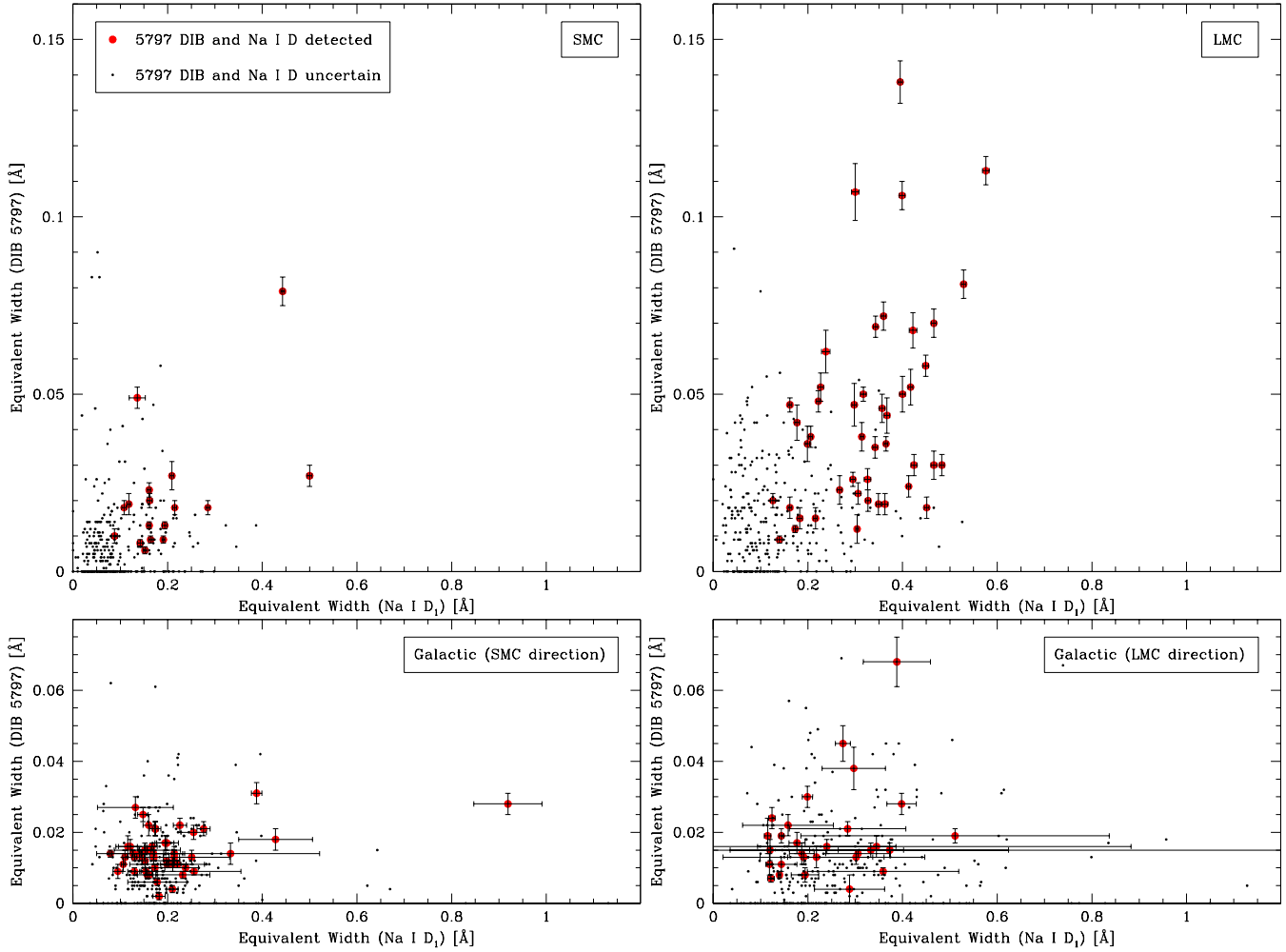


Figure 6. The equivalent width of the 5797 Å DIB versus that of the Na I D₁, for the SMC (*top left*), LMC (*top right*) and the Galactic foreground in the direction of the SMC (*bottom left*) and LMC (*bottom right*).

dence between DIBs and Na I D but not with Ca II K except for a few locations of generally high column density – e.g., the blue component of Ca II K in the South of the Tarantula Nebula and the red component to the West of it.

The maps of the Galactic foreground (Figs. 9 & 10) bear no resemblance to those of the SMC and LMC, which lends credibility to both the Galactic and Magellanic maps we created. In both the SMC and LMC sight-lines the DIBs show gradients over scales of a degree, with possibly smaller scale structure – similar to what was seen in the extra-planar gas in front of the globular cluster ω Centauri by van Loon et al. (2009). For instance, the 5797 Å DIB (Fig. 9) traces a coherent presumably fairly neutral cloud lying across the South-Eastern portion of the SMC field, whereas the 5780 Å DIB identifies material towards the South-Western corner of the LMC field. The EW_{5780}/EW_{5797} ratio is high in places where the 5797 Å DIB is very weak, not where the 5780 Å DIB is strongest. This suggests that the ratio is high in relatively diffuse gas under special conditions.

The foreground Ca II K and especially the Na I D (Fig. 10) is structured with high contrast on much smaller scales, $\sim 0.1^\circ$. This makes it hard to compare these maps with those of the DIBs (Fig. 9), though where the Na I D is strong

(Southern half of the SMC field, around $Dec \sim -69.7^\circ$ in the LMC field) the stronger DIBs are seen also. It is possible that the DIBs are structured on similar small scales as the atomic absorption, but the noise and fewer detections of the much weaker DIBs prevents direct proof.

5 DISCUSSION

5.1 The carriers of the DIBs

The 5780 Å DIB is approximately 2–3 times as strong as the 5797 Å DIB throughout most of the SMC and LMC. This contrasts with the very high ratio of $EW_{5780}/EW_{5797} \sim 6$ found towards R 136, the ionizing cluster of the Tarantula Nebula (van Loon et al. 2013). The latter is an extreme environment and hence not typical of the ambient ISM within the Magellanic Clouds. The $EW_{Na I D1}/EW_{5780} \sim 3$ –4, on the other hand, is very similar between our global maps and the R 136 sight-line. The Local Bubble and its immediate surroundings comprise a typical range of $EW_{5780}/EW_{5797} \sim 2$ –5 (Farhang et al. 2015), concentrated around $EW_{5780}/EW_{5797} \sim 3$ (Bailey et al. 2015), which encompass the ratios found in the Magellanic Clouds. Very

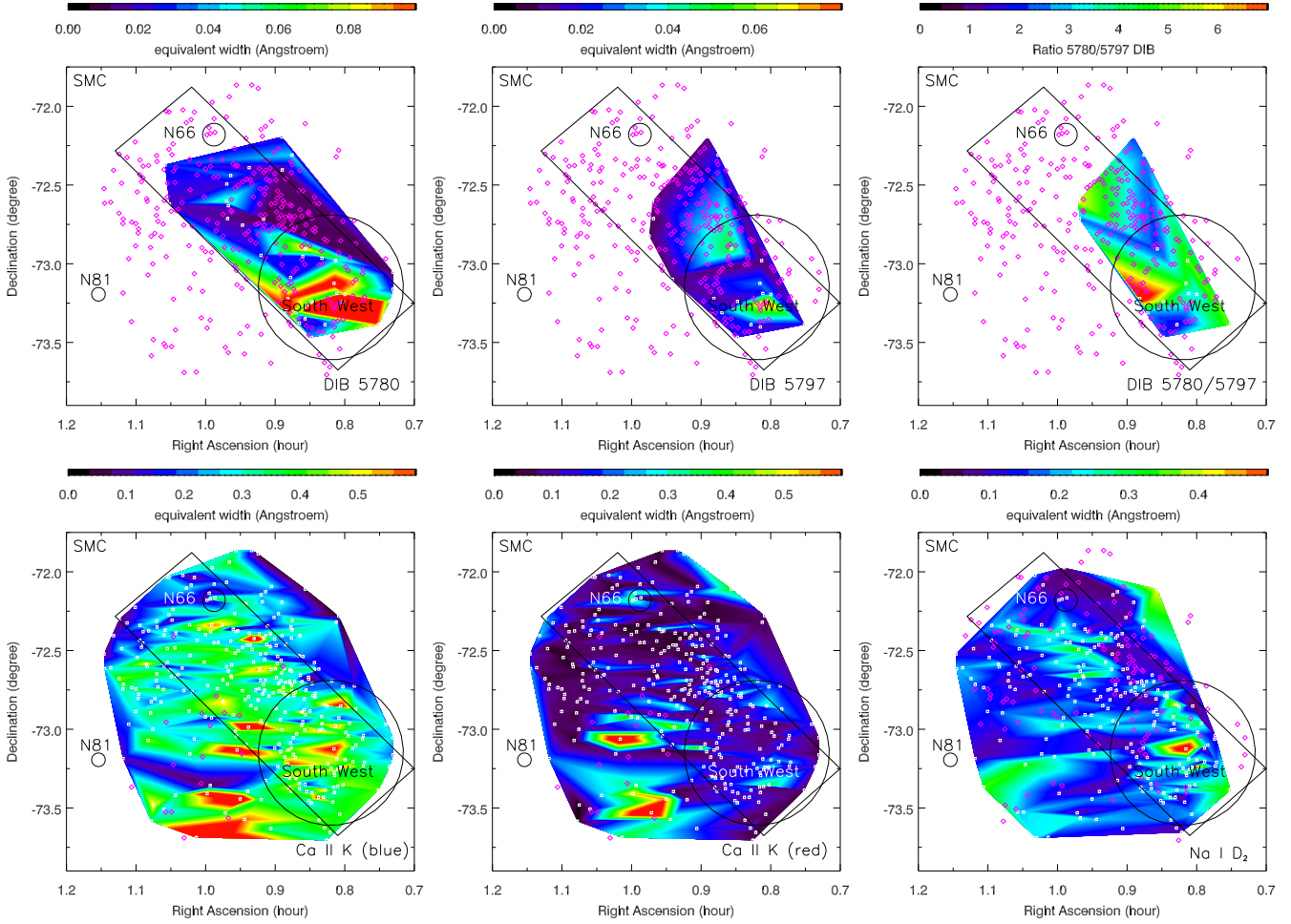


Figure 7. Maps of the SMC in the equivalent width of (*top row*: the 5780 and 5797 Å DIBs and their ratio, and (*bottom row*: the blue and red Ca II K components and Na I D₂). The locations of the target stars are indicated with the small white squares (detections) and magenta diamonds (non-detections).

high values of $EW_{5780}/EW_{5797} \sim 5-9$ are seen *within* the Local Bubble (Bailey et al. 2015); the highest reliable ratios within the Magellanic Clouds are $EW_{5780}/EW_{5797} \sim 7$. The ratio $EW_{NaID1}/EW_{5780} \sim 2-3$ found around the Local Bubble (Farhang et al. 2015) is again commensurate with what is seen across the Magellanic Clouds.

We note that the DIBs are conspicuously weak in the Southern molecular ridge South from 30 Doradus (towards N 158) which is traced by Na I D and (to a lesser degree) Ca II K. This was also noted by van Loon et al. (2013) and may indicate the disappearance (or lack of excitation) of DIB carriers in dense, UV-shielded environments.

The ionization potential of Na⁰ is 5.1 eV, while that of Ca⁰ and Ca⁺ are 6.1 and 11.9 eV, respectively. Comparing this to the ionization potential of H⁰, 13.6 eV, it is clear that in H II regions neither Na I nor Ca II correspond to the dominant stage of ionization. However, in cooler, generally neutral clouds Ca II will diminish with respect to Na I, which is further compounded due to depletion of calcium atoms into grains. It is not yet clear whether DIB carriers survive when immersed in photon baths of > 6 eV, so mapping the DIBs alongside the Na I and Ca II may elucidate this point. Our maps show that the 5780 and 5797 Å DIBs more closely trace Na I than Ca II, with the 5797 Å DIB tracing

cooler and/or more shielded structures than the 5780 Å DIB does. This suggests that the carrier of the 5780 Å DIB is removed by particles/photons with energies in excess of 6 eV, while the carrier of the 5797 Å DIB is already removed at energies in excess of 5 eV. As the 5780 Å DIB stops growing in tandem with the 5797 Å DIB for large column densities, the carrier of the 5780 Å DIB probably needs to be sustained by particles/photons with energies of a few eV, making it likely to be a cation.

Remarkably, the equivalent-width diagrams of either the 5780 or 5797 Å DIB versus Na I D (Figs. 5 & 6) are indistinguishable between the SMC and LMC but for the fewer sight-lines with strong absorption in any of these tracers (an observation which is facilitated by our decision to plot all diagrams between SMC, LMC and Galactic foreground on exactly the same scale). Figure 11 shows this for the 5780 Å DIB, by comparing all good ($> 10\sigma$) detections between the SMC, LMC and Galactic foreground in one graph. This implies that any metallicity dependence affects both sodium and DIB carriers in essentially the same manner. This is very curious, especially if the carriers of the DIBs are complex molecules. In that case one would expect a stronger than linear relation between overall metal content and DIB carrier. As the sodium atomic abundance scales ap-

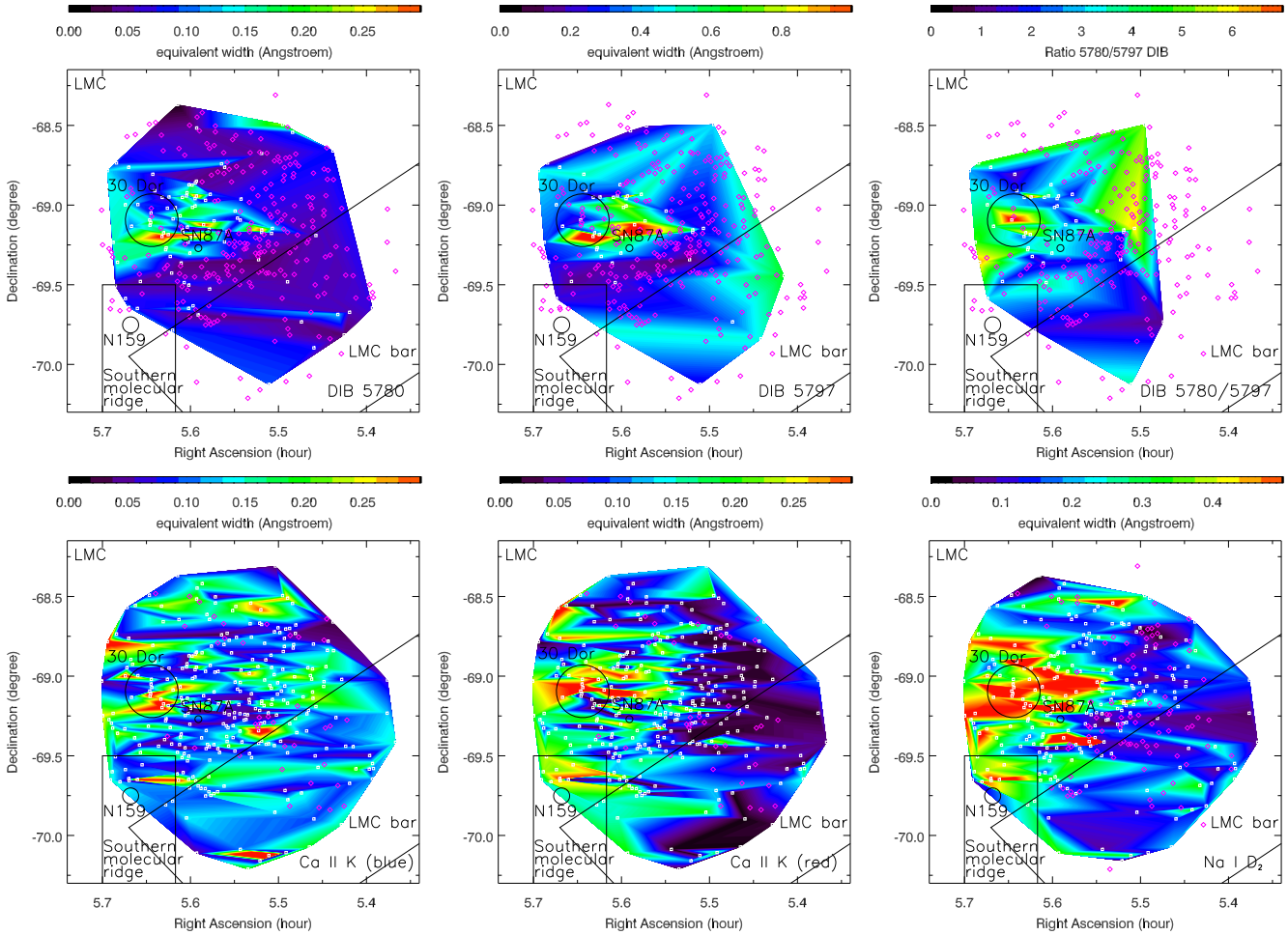


Figure 8. As figure 7, but for the LMC.

proximately in proportion to metallicity, apparently so does the DIB carrier. It means, in turn, that if the DIB carriers are indeed multi-atomic compounds their formation must be efficient and largely complete and this material must be resilient. For instance if they are carbon-based, for instance in the form of fullerenes, then much of the interstellar carbon must be locked within the DIB carriers.

5.2 Structure of the Galactic and Magellanic ISM

The Galactic foreground maps of 5780 and 5797 Å DIBs and Ca II K and Na I D absorption reveal structures on multiple scales – up to a degree down to as small as $\sim 0.1^\circ$, which for typical distances $d \sim 200$ pc means linear scales of ~ 0.35 – 3 pc. The same has been seen in both DIBs and Na I D through extra-planar sight-lines (van Loon et al. 2009), and in Ca II K and Na I D through intermediate- and high-velocity clouds (IVCs and HVCs, respectively; Smoker, Fox & Keenan 2015). Curiously, the correlation between the two DIBs, or Ca II and Na I, is very weak at best – the maps show no conspicuous relationship between each of these pairs of tracers. This suggests that where correlations do exist it is likely due to the cumulative effect of a superposition of structures in a multi-phase ISM in which each individual structure is dominated by one or the other.

The leading edge of the LMC is dense in both Na^0 and Ca^+ . The DIBs are strongest in the star forming regions to the South and West of the Tarantula Nebula; they clearly trace the warmer – but not strongly-irradiated – cloud layers. This is different from both dense, UV-shielded molecular cloud tracers such as CO and far-IR emission on the one hand (or reddening – cf. Tatton et al. 2013), and photo-dissociation regions on the other hand. It would be interesting to see how well DIBs correlate with the unidentified IR emission features commonly attributed to polycyclic aromatic hydrocarbon molecules.

The Na^0 velocities within the LMC cluster around ~ 280 km s^{-1} , down to ~ 240 km s^{-1} . The red “LMC” Ca^+ component is mostly found at velocities ~ 280 km s^{-1} , i.e. associated with the bulk of the Na^0 . We can thus conclude that this absorption arises within the LMC. The blue “LMC” Ca^+ component is mostly found around ~ 220 km s^{-1} , i.e. outside the Na^0 range. In contrast, it is the blue “SMC” Ca^+ component which coincides with the ~ 140 km s^{-1} of the Na^0 within the SMC, whereas the red “SMC” Ca^+ component is found around 200–220 km s^{-1} .

The similarity between the blue “LMC” and red “SMC” Ca^+ kinematics, and their weaker spatial resemblance to the Magellanic Clouds, suggests that this complex is not internal to the Magellanic Clouds, but instead arises within the

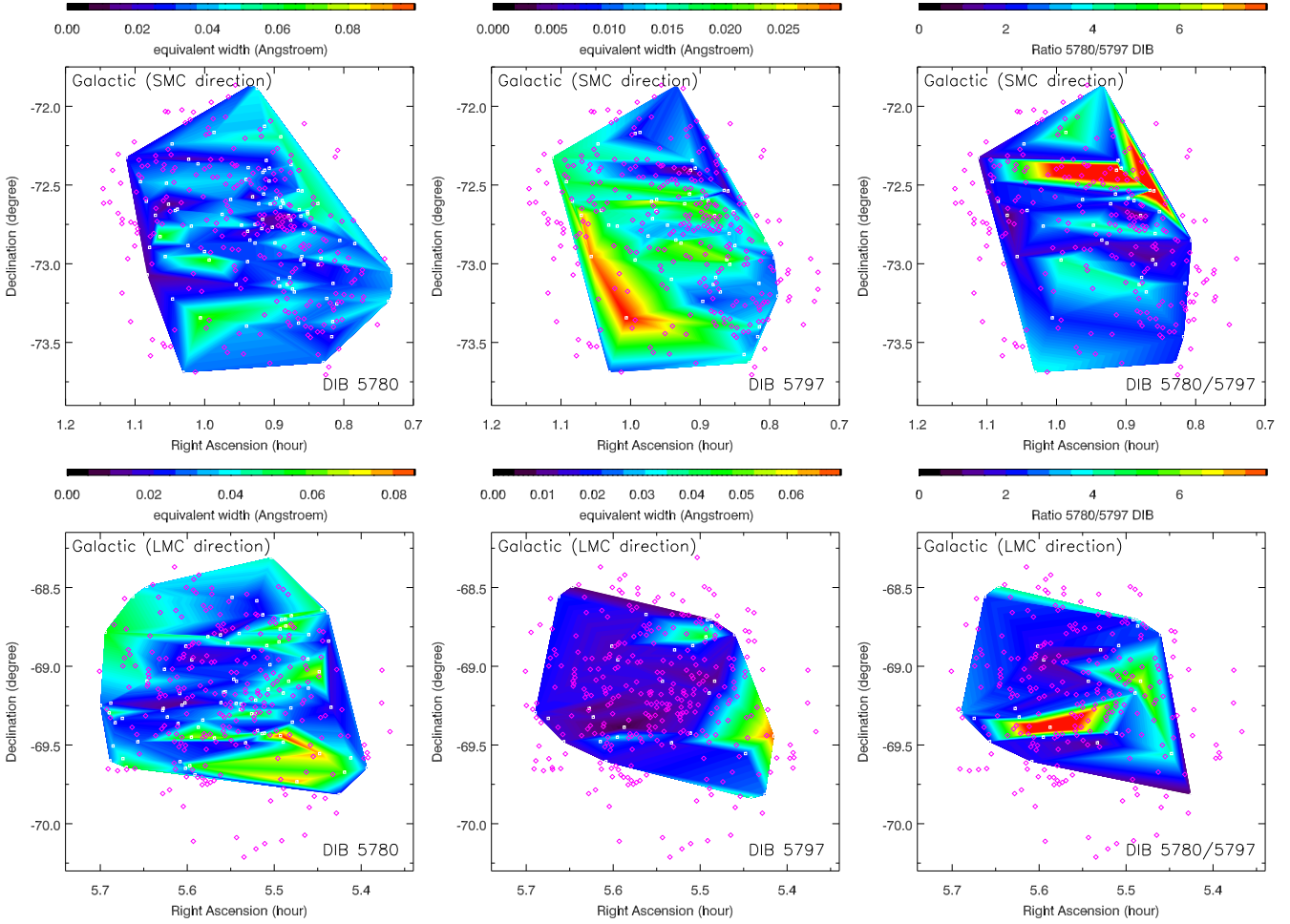


Figure 9. Maps in the equivalent width of the 5780 and 5797 Å DIBs, and their ratio, for the Galactic foreground in the direction of (*top row*: the SMC and *bottom row*: the LMC). The locations of the target stars are indicated with the small white squares (detections) and magenta diamonds (non-detections).

Milky Way Halo. De Boer, Koornneef & Savage (1980) suggested that UV absorption seen in front of the LMC at 220 km s^{-1} has its origin within coronal gas associated with the LMC. Ca II absorption was already detected down to such low velocities towards 30 Doradus by Blades & Meaburn (1980), and a $\sim 200 \text{ km s}^{-1}$ component was seen in H I towards the LMC and Magellanic Stream by McGee, Newton & Morton (1983). Intermediate- and high-velocity clouds such as those populating the Halo are generally transparent in Na I and show up much better in Ca II (Smoker et al. 2015) – hence perhaps why we noticed additional Ca II components but not in Na I. The fact that we detect this kinematic component even towards the SMC suggests that the gas is not solely connected with an LMC corona but perhaps forms part of a pan-Magellanic halo, possibly associated with the putative common dark matter halo invoked by Bekki (2008).

6 SUMMARY OF CONCLUSIONS

We conducted a high signal-to-noise spectroscopic survey of 666 early-type stars within the SMC and LMC, and measured the absorption strength of the 5780 and 5797 Å DIBs and of Ca II K and Na I. We examined correlations between

these different ISM tracers and constructed for the first time maps covering much of these galaxies. Our findings are:

- The 5780 Å DIB is found in more strongly irradiated and/or hotter environments than the 5797 Å DIB, but it too disappears when conditions become too extreme. Both DIBs are depleted in dense molecular clouds.
- The 5780 and 5797 Å DIBs have similar strength w.r.t. Na I in the SMC, LMC and Milky Way. This suggests that the abundance of their carriers is directly proportional to overall metallicity.
- At low column densities, structure is seen at sub-pc scales in all the above tracers, and their correlations exhibit large scatter. Good correlations between different tracers seen in denser columns are probably due at least in part to the averaging effect of multiple, distinct structures along the sight-line even if different conditions prevail within them.
- A common kinematic component around $200\text{--}220 \text{ km s}^{-1}$ is seen in the Ca II K line towards both Magellanic Clouds, suggesting it arises in a pan-Magellanic halo.

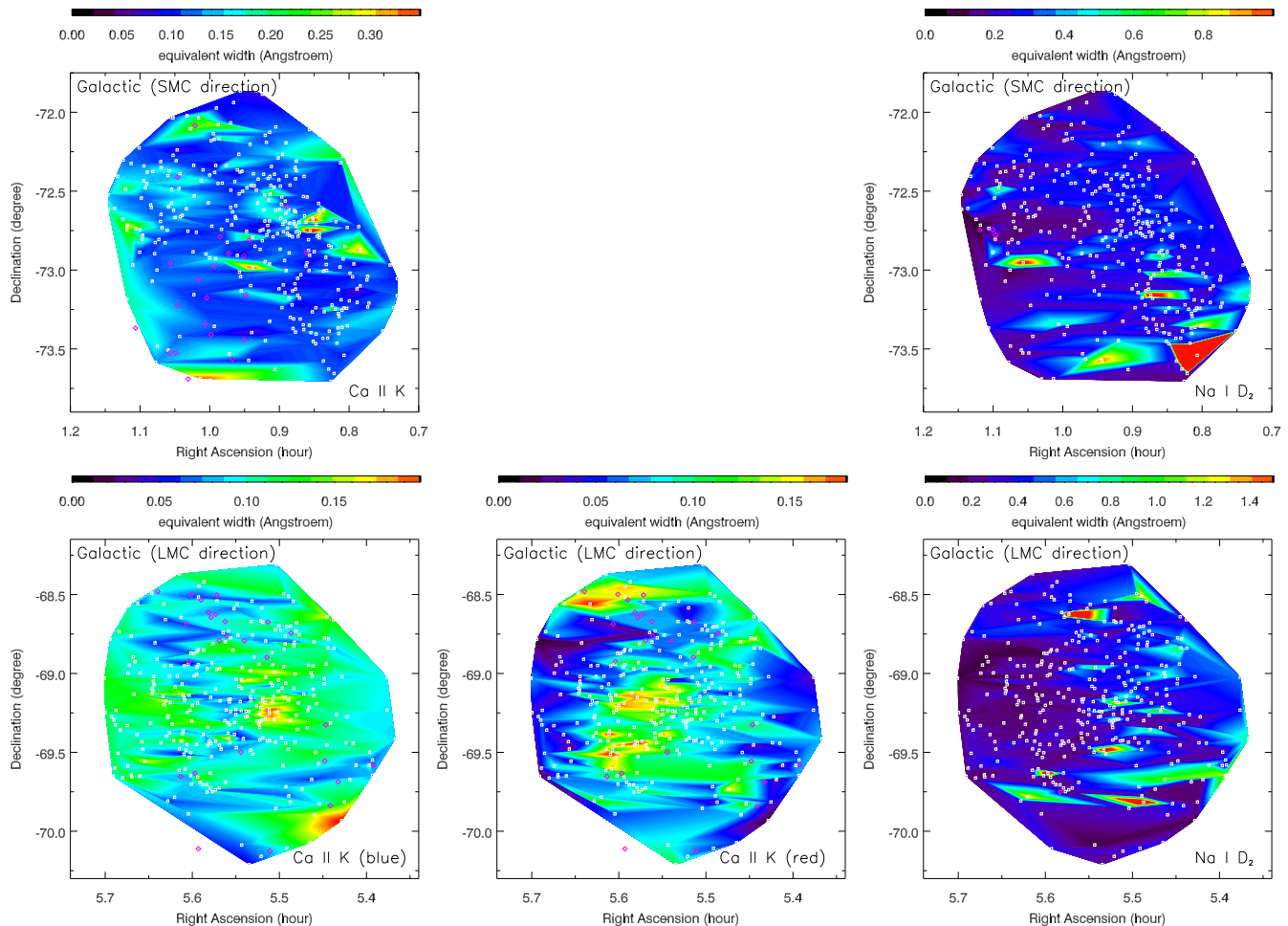


Figure 10. As figure 9 but for Ca II K and Na I D₂.

ACKNOWLEDGMENTS

We thank Chris Evans for reading and commenting on an earlier version of the manuscript, and the referee Francis Keenan for his positive (and swift) report. MB acknowledges support from an STFC studentship at Keele University. PJS thanks the Leverhulme Trust for the award of a Research Fellowship. The AAT observing time was awarded under the European Union funded OPTICON programme. This research has made use of the SIMBAD database, operated at CDS, Strasbourg, France.

REFERENCES

- Azzopardi M., Vignieu J., 1979, A&AS, 35, 353
 Azzopardi M., Vignieu J., Macquet M., 1975, A&AS, 22, 285
 Bailey M., van Loon J.Th., Farhang A., Javadi A., Khosroshahi H.G., Sarre P.J., Smith K.T., 2015, A&A
 Bekki K., 2008, ApJ, 684, L87
 Blades J.C., Madore B.F., 1979, A&A, 71, 359
 Blades J.C., Meaburn J., 1980, MNRAS, 190, P59
 Bonanos A.Z., Lennon D.J., Köhlinger F., et al., 2010, AJ, 140, 416
 Bosch G., Selman F., Melnick J., Terlevich R., 2001, A&A, 380, 137
 Campbell E.K., Holz M., Gerlich D., Maier J.P., 2015, Nature, 523, 322
 Cox N.L.J., Cordiner M.A., Cami J., Foing B.H., Sarre P.J., Kaper L., Ehrenfreund P., 2006, A&A, 447, 991
 Cox N.L.J., Cordiner M.A., Ehrenfreund P., et al., 2007, A&A, 470, 941
 de Boer K.S., Koornneef J., Savage B.D., 1980, ApJ, 236, 769
 Ehrenfreund P., Cami J., Jiménez-Vicente J., et al., 2002, ApJ, 576, L117
 Evans C.J., Howarth I.D., 2008, MNRAS, 386, 826
 Evans C.J., Howarth I.D., Irwin M.J., Burnely A.W., Harries T.J., 2004, MNRAS, 353, 601
 Evans C.J., Lennon D.J., Smartt S.J., Trundle C., 2006, A&A, 456, 623
 Evans C.J., van Loon J.Th., Hainich R., Bailey M., 2015, arXiv:1508.03490
 Farhang A., Khosroshahi H.G., Javadi A., et al., 2015, ApJ, 800, 64
 Fariña C., Bosch G.L., Morrell N.I., Barbá R.H., Walborn N.R., 2009, AJ, 138, 510
 Garmany C.D., Conti P.S., Massey P., 1987, AJ, 93, 1070
 Garmany C.D., Massey P., Parker J.Wm., 1994, AJ, 108, 1256
 Grebel E.K., Roberts W.J., Brandner W., 1996, A&A, 311, 470
 Houziaux L., Nandy K., Morgan D.H., 1980, A&A, 84, 377
 Hunter I., Lennon D.J., Dufton P.L., Trundle C., Simón-Díaz S., Smartt S.J., Ryans R.S.I., Evans C.J., 2008, A&A, 479, 541
 Jenniskens P., Désert F.-X., 1994, A&AS, 106, 39
 Johnson H.L., 1963, in: "Basic Astronomical Data: Stars and stel-

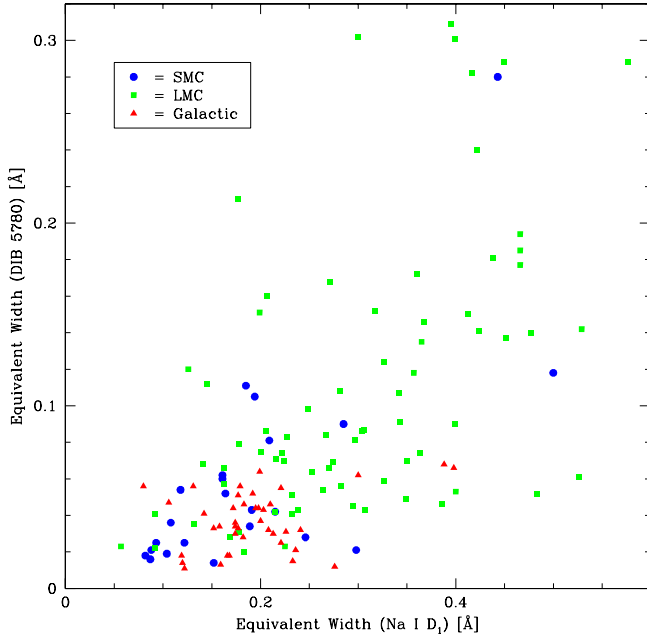


Figure 11. The equivalent width of the 5780 Å DIB versus that of the Na I D₁, for the SMC (blue circles), LMC (green squares) and the Galactic foreground (red triangles). Only $> 10\sigma$ detections are plotted.

lar systems”, ed. K.A. Strand (University of Chicago Press), p.204
 Keenan F.P., Conlon E.S., Brown P.J.F., Dufton P.L., 1988, *A&A*, 192, 295
 Lamb J.B., Oey M.S., Graus A.S., Adams F.C., Segura-Cox D.M., 2013, *ApJ*, 763, 101
 Madore B.F., 1982, *ApJ*, 253, 575
 Martayan C., Frémat Y., Hubert A.-M., Floquet M., Zorec J., Neiner C., 2007, *A&A*, 462, 683
 Massey P., 2002, *ApJS*, 141, 81
 Massey P., Parker J.Wm., Garmany C.D., 1989, *AJ*, 98, 1305
 Massey P., Waterhouse E., DeGioia-Eastwood K., 2000, *AJ*, 119, 2214
 Massey P., Morrell N.I., Neugent K.F., Penny L.R., DeGioia-Eastwood K., Gies D.R., 2012, *ApJ*, 748, 96
 McEvoy C.M., Dufton P.L., Evans C.J., et al., 2015, *A&A*, 575, 70
 McGee R.X., Newton L.M., Morton D.C., 1983, *MNRAS*, 205, 1191
 Mihalas D., 1973, *ApJ*, 179, 209
 Parker J.Wm., 1993, *AJ*, 106, 560
 Paul K.T., Subramaniam A., Mathew B., Mennickent R.E., Sabogal B., 2012, *MNRAS*, 421, 3622
 Reid W.A., Parker Q.A., 2012, *MNRAS*, 425, 355
 Ridley J.P., Crawford F., Lorimer D.R., Bailey S.R., Madden J.H., Anella R., Chennamangalam J., 2013, *MNRAS*, 433, 138
 Rivero González J.G., Puls J., Najarro F., Brott I., 2012, *A&A*, 537, 79
 Sabín-Sanjulián C., Simón-Díaz S., Herrero A., et al., 2014, *A&A*, 564, 39
 Sanduleak N., 1970, *Contr. Cerro-Tololo Obs.*, 89 1
 Schild H., Testor G., 1992, *A&AS*, 92, 729
 Smoker J.V., Fox A.J., Keenan F.P., 2015, *MNRAS*, 451, 4346
 Tatton B.L., van Loon J.Th., Cioni M.-R., et al., 2013, *A&A*, 554, 33
 Testor G., Niemela V., 1998, *A&AS*, 130, 527

Table A1. Pertinent literature sources for the spectral types, in chronological order (by year, then alphabetical).

<i>SMC:</i>	
Azzopardi, Vigneau & Macquet	(1975)
Azzopardi & Vigneau	(1979)
Garmany, Conti & Massey	(1987)
Massey, Parker & Garmany	(1989)
Grebel, Roberts & Brandner	(1996)
Evans et al.	(2004)
Evans et al.	(2006)
Martayan et al.	(2007)
Evans & Howarth	(2008)
Hunter et al.	(2008)
Bonanos et al.	(2010)
Paul et al.	(2012)
Lamb et al.	(2013)
Ridley et al.	(2013)
<i>LMC:</i>	
Sanduleak	(1970)
Schild & Testor	(1992)
Parker	(1993)
Garmany, Massey & Parker	(1994)
Testor & Niemela	(1998)
Massey, Waterhouse & DeGioia-Eastwood	(2000)
Bosch et al.	(2001)
Fariña et al.	(2009)
Walborn et al.	(2010)
Weidner & Vink	(2010)
Massey et al.	(2012)
Reid & Parker	(2012)
Rivero González et al.	(2012)
Sabín-Sanjulián et al.	(2014)
McEvoy et al.	(2015)
Evans et al.	(2015)

van Loon J.Th., Smith K.T., McDonald I., Sarre P.J., Fossey S.J., Sharp R.G., 2009, *MNRAS*, 399, 195
 van Loon J.Th., Bailey M., Tatton B.L., et al., 2013, 550, A108
 Walborn N.R., Howarth I.D., Evans C.J., et al., 2010, *AJ*, 139, 1283
 Weidner C., Vink J.S., 2010, *A&A*, 524, 98
 Welty D.E., Federman S.R., Gredel R., Thorburn J.A., Lambert D.L., 2006, *ApJS*, 165, 138
 Wenger M., Ochsenbein F., Egret D., et al., 2000, *A&AS*, 143, 9

APPENDIX A: SPECTRAL TYPES

We performed a search in the literature for known spectral types, thereby mostly relying on the use of SIMBAD (Wenger et al. 2000); a summary of the pertinent sources for these spectral types is presented in table A1. These spectral types have been included in our catalogue, and comprise 174 SMC and 61 LMC targets. Their distribution over spectral type and luminosity class is presented in figure A1. The more extensive coverage of the SMC includes also more later (A) type stars, whilst the known spectral types for LMC sources tend to include more O-type classes. Most of the targets with known spectral type are mid-B (SMC) or early-B (LMC).

The question arises concerning the contribution from stellar photospheric absorption to the measurements of the calcium and sodium lines. Indeed, equivalent widths of the Ca II K line can reach 0.1–0.2 Å at solar metallicity (Mihalas

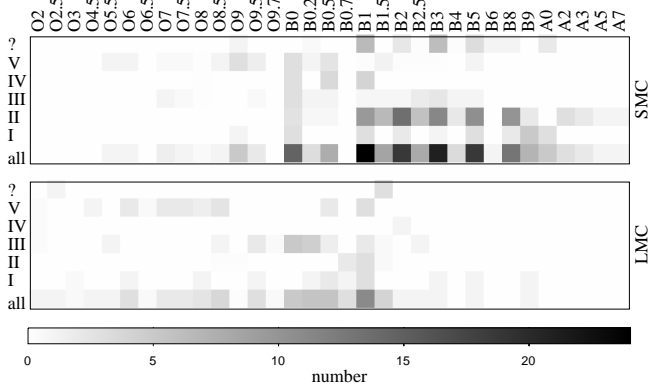


Figure A1. Distribution over spectral type and luminosity class, for the (*top:*) SMC and (*bottom:*) LMC.

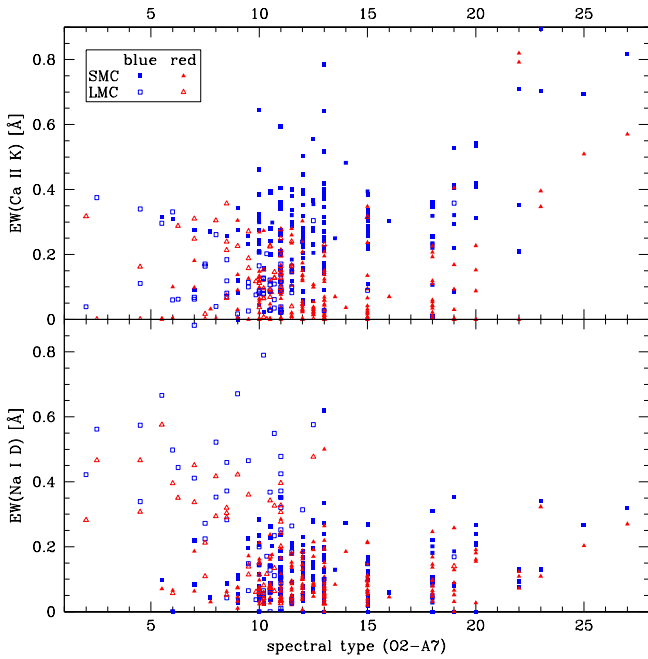


Figure A2. Distribution over spectral type and luminosity class, for the (*top:*) SMC and (*bottom:*) LMC.

1973; Keenan et al. 1988). Figure A2, however, exhibits no dependence of the Ca II K absorption on spectral type, except perhaps for the A type stars that seem to have larger equivalent widths (but that are few in number). The equivalent width of the stronger (blue) kinematic component is mostly 0.2–0.4 Å and thereby larger than what is expected for the stellar photosphere of (metal-poor) O- and B-type stars; the other (red) kinematic component is often much weaker but the same insensitivity to spectral type holds true. The same conclusion is reached for the Na I D₂ (blue) and D₁ (red) lines (bottom panel in figure A2).

We can also remark that the Ca II K absorption is of similar strength in the SMC and LMC, whereas we would have expected a clear difference if it mainly originated in the stellar photospheres due to the considerable difference in metallicity between the young populations of the SMC and LMC. The Na I D absorption, on the other hand, does

show the expected scaling with metallicity – but this can also be explained if it were of purely interstellar origin.

This all appears to be rather reassuring and lends credibility to the analysis of the ISM absorption. Spectral typing of the remainder of the target sample will be the subject of a forthcoming paper.